REPORT

SPINTRONICS

Relativistic kinematics of a magnetic soliton

Lucas Caretta[1], Se-Hyeok Oh[2], Takian Fakhrul[1], Dong-Kyu Lee[3], Byung Hun Lee[1], Se Kwon Kim[4], Caroline A. Ross[1], Kyung-Jin Lee[2,3,4,5], Geoffrey S. D. Beach[1]*

A tenet of special relativity is that no particle can exceed the speed of light. In certain magnetic materials, the maximum magnon group velocity serves as an analogous relativistic limit for the speed of magnetic solitons. Here, we drive domain walls to this limit in a low-dissipation magnetic insulator using pure spin currents from the spin Hall effect. We achieve record current-driven velocities in excess of 4300 meters per second—within ~10% of the relativistic limit—and we observe key signatures of relativistic motion associated with Lorentz contraction, which leads to velocity saturation. The experimental results are well explained through analytical and atomistic modeling. These observations provide critical insight into the fundamental limits of the dynamics of magnetic solitons and establish a readily accessible experimental framework to study relativistic solitonic physics.

In 1905, Einstein showed that Newtonian mechanics based on Galilean invariance breaks down at high speeds (*1*). Instead, the speed of light c serves as a fundamental limit irrespective of the reference frame of the observer, ensured by Lorentz contraction and time dilation in Einstein's special theory of relativity. In certain condensed matter systems—such as dislocations in crystals (*2*), charge density waves (*3*), and magnetic domain walls (*4*–*12*)—space and time variables are related in such a way that the dynamics of solitonic quasiparticles can mimic relativistic kinematics. The excitations in such systems can be described by the Lorentz-invariant sine-Gordon equation (*4*)

$$\frac{\partial^2\theta}{\partial t^2} - c_m^2\frac{\partial^2\theta}{\partial x^2} + \frac{c_m^2}{\Delta_0^2}\sin\theta = 0 \qquad (1)$$

where Δ_0 is a characteristic length scale and c_m is a characteristic speed. The space (x) and time (t) variables transform through the Lorentz factor $\gamma' = (1 - v^2/c_m^2)^{-1/2}$ under a Lorentz boost at a velocity v, and hence c_m plays a role analogous to c in the theory of special relativity (*4*–*6*).

Under certain conditions, the spin excitations in a magnet can be mapped to Eq. 1 by treating the lattice as a continuum (supplementary text S1). This has been shown, for example, for uniaxial ferromagnets (*4*–*6*), antiferromagnets (*7*, *8*, *10*, *11*, *13*), and ferrimagnets (*12*). In this context, Δ_0 is the equilibrium domain wall (DW) width, $c_m \equiv v_g^{max}$ is the maximum magnon group velocity, and $\theta/2$ is the polar magnetization angle (the azimuthal angle can be integrated out for stationary states, as shown in supplementary text S1). The relativistic nature of the field dynamics in Eq. 1 is naturally inherited by the dynamics of its nonlinear solitonic solution, a traveling DW $\theta(x,t) = 4\tan^{-1}\left[\exp\left(\frac{x-vt}{\Delta}\right)\right]$, which behaves like a relativistic free particle (*5*) whose velocity v is ultimately bounded by v_g^{max} (*5*, *9*, *10*, *12*–*14*). The DW profile resembles the usual Walker ansatz (*15*) but with a Lorentz-contracted DW width, $\Delta = \Delta_0/\gamma'$.

Dissipation and driving terms are straightforward to include in Eq. 1 (supplementary text S1), with the modified Walker ansatz remaining an exact solution (*6*, *9*–*12*). For a sine-Gordon DW in a uniaxial ferromagnet with an easy-axis drive field H and Gilbert damping α, one finds $v = (\gamma\Delta/\alpha)H$, where γ is the gyromagnetic ratio (*6*). For ferrimagnets, α and γ are replaced by scaled parameters α_{eff} and γ_{eff}, respectively (*16*–*18*), which permit the coupled sublattices to be described through a single (Néel) order parameter (*12*) (materials and methods). For small v, this coincides with Walker's classical (*15*) stationary-state solution $v_0 = (\gamma\Delta_0/\alpha)H$. Replacing Δ_0 by Δ corresponds to a high-velocity correction $v = v_0\sqrt{1-(v/v_g^{max})^2}$, which, when rearranged to read $v = v_g^{max}/\sqrt{1+(v_g^{max}/v_0)^2}$, makes clear that v can never exceed v_g^{max}. Strictly speaking, dissipation breaks Lorentz invariance because it derives from motion with respect to the lattice, which implies that these relativistic transformations hold only for an observer at rest with respect to the magnet.

Relativistic dynamics is, in practice, inaccessible in ferromagnets, in which large damping limits the DW mobility and dynamical

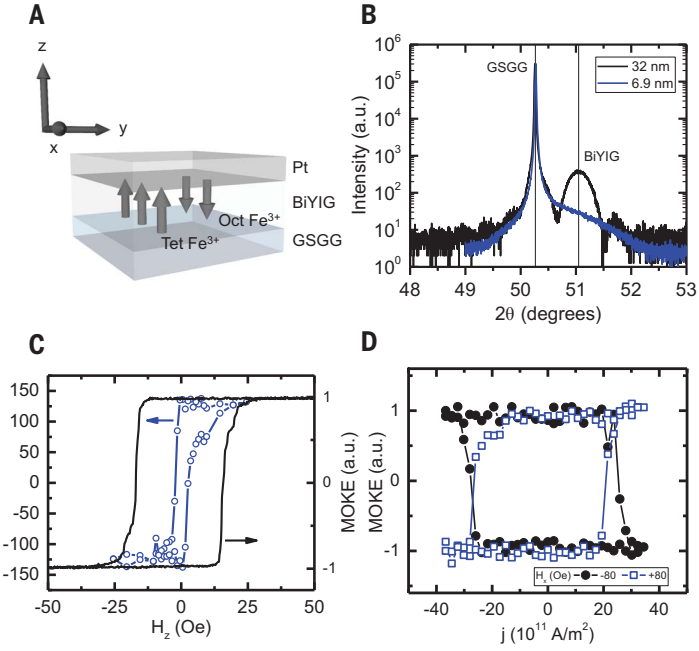

Fig. 1. Structural and magnetic characterization. (**A**) Schematic of $Gd_3Sc_2Ga_3O_{12}$ (GSGG)/BiYIG/Pt trilayer structure. Arrows indicate the orientation of the tetrahedral (Tet) and octahedral (Oct) site Fe^{3+} magnetic moments in BiYIG. (**B**) High-resolution x-ray diffraction (2θ – ω scan) of 32-nm thick (black) and 6.9-nm thick (blue) GSGG/BiYIG. (**C**) VSM (blue, left axis) and MOKE (black, right axis) hysteresis loops of a perpendicularly magnetized GSGG/BiYIG (6.9 nm) film. (**D**) Current-induced switching probed via MOKE in GSGG/BiYIG (6.9 nm)/Pt (4.0 nm). M_S, saturation magnetization; a.u., arbitrary units; emu, electromagnetic unit; cc, cubic centimeter.

[1]Department of Materials Science and Engineering, Massachusetts Institute of Technology (MIT), Cambridge, MA 02139, USA. [2]Department of Nano-Semiconductor and Engineering, Korea University, Seoul 02841, Korea. [3]Department of Materials Science and Engineering, Korea University, Seoul 02841, Korea. [4]Department of Physics, Korea Advanced Institute of Science and Technology (KAIST), Daejeon 34141, Korea. [5]KU-KIST Graduate School of Converging Science and Technology, Korea University, Seoul 02841, Korea.
*Corresponding author. Email: gbeach@mit.edu

instabilities such as Walker breakdown (*6*, *15*, *19*) typically set in far below v_g^{max}. However, in antiferromagnets and ferrimagnets, precessional dynamics is suppressed (*17*, *20*, *21*) and the possibility of relativistic kinematics under experimentally realizable conditions has recently been predicted (*10*–*12*, *22*). Here, we show that in a low-dissipation ferrimagnetic iron garnet, current-induced torques can drive DWs to relativistic speeds in excess of 4300 m/s, limited by Lorentz contraction of the DW width as v asymptotically approaches the magnonic limit. Our experimental results are supported by analytical and atomistic modeling of the dynamics, which account well for our observations. These results provide insights into the ultimate speed of magnetic quasiparticle excitations—and hence the operating speed of spintronic devices that utilize them (*23*, *24*)—and introduce an arena for relativistic solitonic physics that puts related phenomena such as terahertz spin-wave radiation (*12*) within experimental reach.

We examined DW dynamics at room temperature in 6.9-nm thick epitaxial bismuth-substituted yttrium iron garnet (BiYIG) (Fig. 1A and materials and methods), a perpendicularly magnetized ferrimagnetic insulator with low damping (*25*) to facilitate a high DW mobility. A thin Pt overlayer was used to generate a current-induced torque via the spin Hall effect (SHE) (*26*–*30*), which has recently been shown to allow for current-induced switching and fast DW motion in rare earth iron garnets (*31*–*33*). Figure 1B shows exemplary x-ray diffraction results that illustrate fully strained film growth with high structural quality. Perpendicular magnetic anisotropy with near-bulk saturation magnetization was confirmed with vibrating sample magnetometry (VSM) and polar magneto-optical Kerr effect measurements (MOKE) (Fig. 1C and materials and methods). Deterministic magnetization switching via the SHE (Fig. 1D) was verified by injecting current pulses in a lithographically fabricated track (materials and methods). The switching polarity depends on the direction of a longitudinal bias field (Fig. 1D), as expected for damping-like spin-orbit torque.

Current-induced DW motion was imaged in a conventional racetrack geometry (Fig. 2A) using a wide-field MOKE microscope (materials and methods). The damping-like torque from the SHE acts like an easy-axis magnetic field $H_{SHE} = \chi_0 j \cos(\Phi)$ in the DW (*34*, *35*). Here, χ_0 is proportional to the spin Hall angle of Pt, j is the current density, and Φ is the azimuthal DW angle (Fig. 2, A to C). As shown elsewhere (*36*) and in figs. S2 and S6, the Dzyaloshinskii-Moriya interaction in these films is negligible because of the lack of a rare earth ion, and hence the equilibrium DW orientation is Bloch ($\Phi = \pm\pi/2$) (Fig. 2A). As such, the DWs are intrinsically immobile under current injection, but they can be driven by H_{SHE} in the presence of a longitudinal bias field H_x, which induces a Néel character (Fig. 2, B and C). Figure 2D shows a series of MOKE images after sequential current pulse injection under finite H_x, which verifies the current-driven motion and allows the DW velocity to be extracted (materials and methods and supplementary text S2).

Figure 2E shows $v(j)$ curves measured for several values of H_x. In all cases, v first increases with increasing j and then saturates toward a maximum velocity, v_{sat}. This limiting velocity scales linearly with H_x up to ~100 Oe (Fig. 2F), beyond which v tends to an apparent global maximum that is insensitive to both j and H_x. Measurements on a thinner 2.4-nm BiYIG sample (supplementary text S3 and fig. S6) showed similar saturation behavior. The low-H_x behavior is well understood and follows from the usual one-dimensional model of torques (*34*, *35*). The driving field $H_{SHE}\,\hat{z}$ exerts a torque on the DW moment m_{DW}, which cants it away from the field $H_x\,\hat{x}$ that sets its equilibrium orientation (Fig. 2C). This results in a restoring torque in the direction $m_{DW} \times \hat{x}$ that pulls the magnetization toward the easy-axis driving field, which causes the DW to move while the preferred adjacent domain grows. The DW velocity is thus proportional to the restoring torque $\propto H_x \sin(\Phi)$,

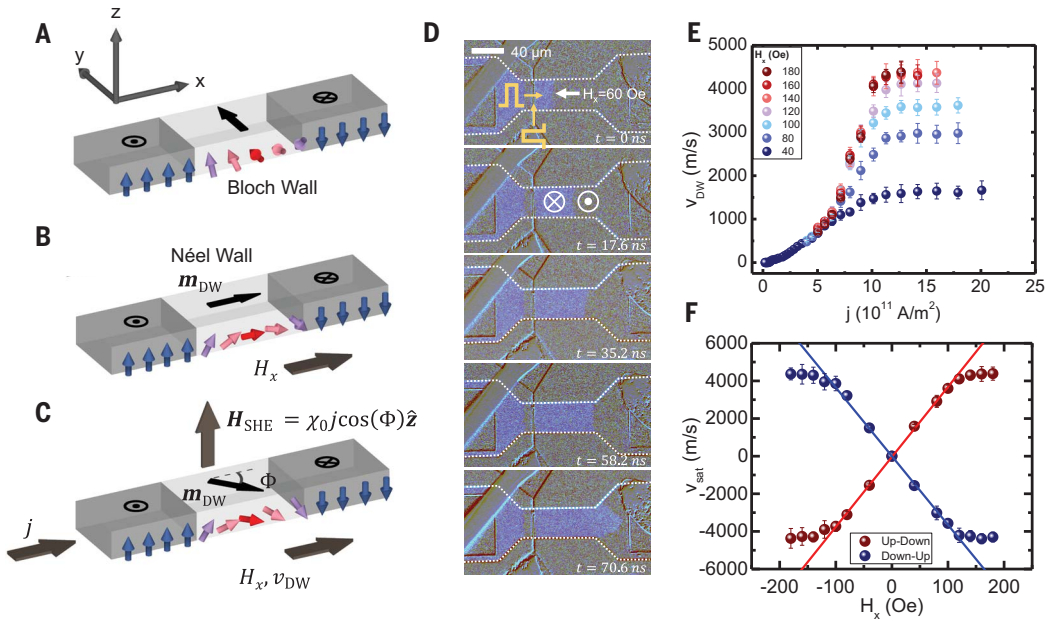

Fig. 2. Relativistic DW motion. (**A**) Schematic of the equilibrium DW structure in GSGG/BiYIG (6.9 nm)/Pt (4.0 nm) (substrate and Pt overlayer excluded for clarity). The dark gray regions represent magnetic domains, whereas the light gray region signifies the DW. Two-dimensional black vectors illustrate the magnetic moment in each region, and the overlaid three-dimensional arrows detail the local moment orientation traversing the DW. (**B**) DW moment m_{DW} under an applied longitudinal in-plane field $H_x\,\hat{x}$. (**C**) Equilibrium DW orientation Φ when traveling at velocity v_{DW} under applied $H_x\,\hat{x}$ and driven by $H_{SHE} = \chi_0 j \cos\Phi\hat{z}$. (**D**) Time-stamped MOKE microscopy depicting current-driven DW motion in BiYIG. Contrast in the image (bright versus dark) corresponds to the net magnetization orientation (into the plane versus out of the plane), and the dashed white lines outline the DW racetrack. DW nucleation and drive currents are depicted in yellow. A train of drive pulses with current density $j \sim 1.65 \times 10^{12}$ A/m^2 was injected between each image frame. (**E**) DW velocity v_{DW} versus j for various H_x. (**F**) Saturation velocity v_{sat} in the $v_{DW}(j)$ curves in (E) versus H_x. The plotted data points correspond to the velocity at fixed current density $j \sim 1.65 \times 10^{12}$ A/m^2 such that the curve is isothermal considering joule heating. Error bars represent the standard deviation of three independent measurements of the DW velocity.

whose magnitude is maximum as $|\Phi| \rightarrow \pi/2$. This results in an inherent limiting velocity v_{max} that depends on the DW stiffness—that is, the maximum internal restoring torque, as first recognized by Walker (*15*).

For a SHE-driven ferrimagnetic DW, the conventional one-dimensional model predicts (*34*, *35*)

$$v = v_{max}/\sqrt{1 + [\alpha_{eff}\ \pi H_x/2\chi_0 j]^2} \quad (2)$$

with a limiting velocity $v_{max} = \frac{\pi}{2}\gamma_{eff}\ \Delta_0 H_x$ proportional to the stiffness field H_x. This behavior is widely known in the literature (*29*) and is borne out in our $v(j)$ curves at low H_x (Fig. 2E). In this regime, the linear scaling of v_{sat} with H_x (Fig. 2F) identifies the saturation mechanism as the distortion of the DW from Néel to Bloch. However, as H_x is increased beyond 100 Oe, the linear scaling of v_{sat} breaks down. This implies that the maximum DW velocity—which in the usual DW dynamics models is limited only by the restoring torque and is hence unbounded—approaches a more fundamental limit in our experiments. This limit is evidently independent of the restoring torque and therefore cannot be understood in the conventional model framework. However, it can be naturally explained by Lorentz contraction of Δ as $v \rightarrow v_g^{max}$, as we show below.

In a ferrimagnet (*12*), $v_g^{max} = \frac{2A}{dS}$, where A is the exchange constant, d is the interatomic distance, and $S = (|S_1| + |S_2|)$ is the total spin density of the sublattices. Both d and S are known from the structure and number density of moment-bearing Fe^{3+} ions in BiYIG (materials and methods), so to estimate v_g^{max}, we need only determine A, which we have done using Brillouin light scattering (BLS) (*37*–*39*). BLS spectra were collected in Damon-Eshbach (DE) (*40*) geometry (Fig. 3A and materials and methods) using λ = 532 nm laser illumination. An in-plane field $H_x\,\hat{x}$ was applied, and the incident-backscatter light angle θ was varied in the yz plane to select the wave vector transfer $q_{||} = (4\pi/\lambda)\sin(\theta)$. Figure 3B shows BLS spectra at θ = 45° for three BiYIG film thicknesses t, each at three values of H_x. The field dependence (fig. S3) allows one to discriminate between spin wave peaks and peaks of nonmagnetic origin, such as the peak at ~27 GHz, which we attribute to a substrate phonon mode.

The measurement geometry is sensitive to DE magnetostatic surface modes and perpendicular standing spin wave (PSSW) modes (*41*). The former modes are relatively insensitive to t, whereas the latter arise from confinement normal to the film plane and depend markedly on t (*37*, *38*). Thus, we identify the mode that appears in a similar low-frequency range for all t as the DE mode and the high-frequency mode that appears in the 29-nm film as the lowest order PSSW mode, which shifts to inaccesible frequencies for thinner films. In contrast to the DE modes (*39*), the PSSW mode frequency has a dominant exchange contribution because its wave vector $k = \sqrt{q_{||}^2 + \left(\frac{\pi}{t}\right)^2} \approx (9\ \text{nm})^{-1}$ is comparable to the inverse exchange length, so this mode can be used to extract A (*37*, *38*). Figure 3C shows the $q_{||}$ dependence of the DE and PSSW mode frequencies in the t = 29 nm film, along with fits to the well-known DE and PSSW dispersion relations (*41*) (materials and methods), which further supports our mode identification. From the PSSW fit, we extract A = (4.2 ± 0.2) pJ/m, which agrees with the bulk value, 4.15 pJ/m (*16*).

The exchange-mode spin wave dispersion, which is not directly accessible by BLS, can be computed from experimental material parameters (Fig. 4A) using the expression (*12*)

$$\omega_{\pm} = \frac{\pm\delta_s + \sqrt{\delta_s^2 + 4\rho(Ak^2 + K_u)}}{2\rho} \quad (3)$$

where ω is the angular frequency, ± denotes the mode handedness, δ_s is the net spin density, K_u is the uniaxial anisotropy constant (fig. S1), and ρ is the inertia of the dynamics (materials and methods). The estimated maximum magnon group velocity, $v_g^{max} = \frac{2A}{dS}$, is ~5000 m/s, which is comparable to the experimental speed limit in Fig. 2F. This suggests that relativistic corrections to Eq. 2 are required to properly account for the experiments. Equation 2 can be generalized to high velocities by accounting for DW Lorentz contraction $\Delta = \Delta_0\sqrt{1 - (v/v_g^{max})^2}$, analogous to the case of an easy-axis applied field discussed above. By taking the ratio of v_{sat} measured at large H_x to its value at low H_x where $\Delta \approx \Delta_0$, we can estimate the ratio of the dynamical DW width to its static width, Δ/Δ_0, as all other parameters are eliminated in the ratio. In Fig. 4B, we see that the inferred Δ/Δ_0 is reduced at high speeds, which suggests that Lorentz

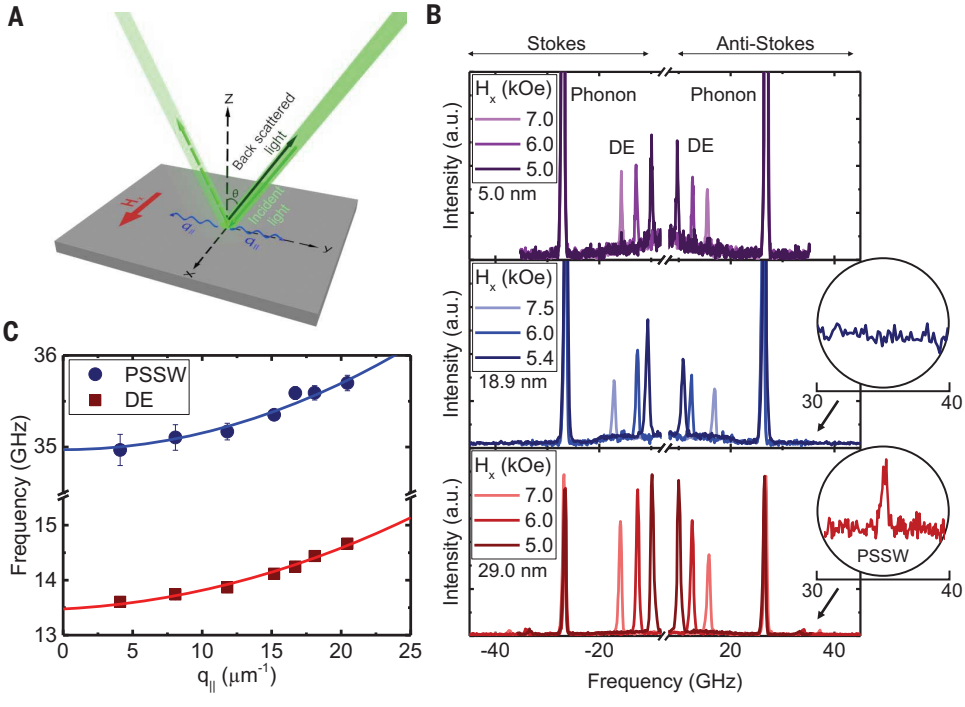

Fig. 3. Exchange constant from BLS. (**A**) Schematic of BLS measurement geometry. (**B**) BLS spectra of GSGG/BiYIG (t) where t = 5.0 nm, 18.9 nm, and 29.0 nm for several in-plane fields H_x at an incident angle of θ = 45°, corresponding to $q_{||} = 16.7 \times 10^6$ rad/m. Circular insets magnify the 30- to 40-GHz regime. (**C**) In-plane wave vector ($q_{||}$) dependence of the DE and PSSW mode peak frequencies under H_x = 6.6 kOe and fits to the dispersion relations. Error bars in (C) are fit uncertainty of the BLS spectra peaks.

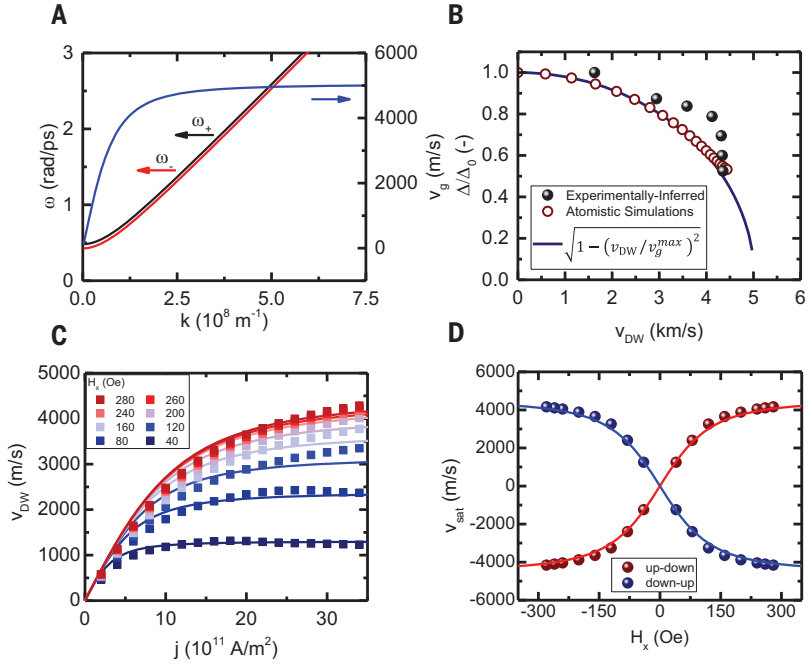

Fig. 4. Modeling of relativistic DW motion. (**A**) Analytically computed dispersion relations (Eq. 3) of exchange-mode spin waves of each handedness and their common group velocity, v_g. Here, k denotes wave vector and ω denotes frequency. (**B**) Dynamical DW width Δ normalized to its equilibrium value Δ_0. Symbols are from atomistic simulations (materials and methods), and orbs correspond to values inferred from the experimental DW velocity data as described in the text. The solid line represents the inverse Lorentz factor, $\sqrt{1-(v_{DW}/v_g^{max})^2}$ with $v_g^{max} \approx 5000$ m/s computed from the exchange constant. (**C**) Analytical (lines, Eq. 4) and atomistic (symbols) modeling of the DW velocity v_{DW} as a function of current density j for various in-plane fields H_x. (**D**) Analytical (lines, Eq. 4) and atomistic (symbols) modeling of the high-j saturation velocity v_{sat} as a function of H_x.

contraction gives rise to the asymptotic velocity maximum in Fig. 2F.

Figure 4, C and D, shows analytical and atomistic modeling that fully accounts for the experimental observations. Inserting the Lorentz-contracted DW width in Eq. 2 and algebraically rearranging the terms, the analytical model reads

$$v = \frac{\tilde{v}}{\sqrt{1+[\tilde{v}/v_g^{max}]^2}} \qquad (4)$$

where $\tilde{v}(j;H_x)$ corresponds to Eq. 2 with the equilibrium DW width Δ_0. We used $\Delta_0 = \sqrt{\frac{A}{K_u}} \approx 14$ nm and $v_g^{max} \approx 5000$ m/s—both estimated from experimentally measured parameters—along with the experimentally measured χ_0 (fig. S2 and materials and methods) and dynamical parameters, α_{eff} and γ_{eff}, estimated from the low-j slope and high-j saturation of $v(j)$ at small H_x (materials and methods). Figure 4, C and D, shows that Eq. 4 reproduces all key features in Fig. 2, E and F, although the discrepancy in the low-j regime for $v(j)$ suggests some impact of disorder (pinning). We also performed two-sublattice atomistic simulations of the current-driven motion for a one-dimensional ferrimagnetic system, using atomistic parameters that correspond to the continuum material parameters in the analytical model (materials and methods). We find excellent quantitative agreement between the analytical model and the full atomistic simulations, as seen in Fig. 4, B to D. Particularly, the predicted Lorentz contraction of the DW width is quantitatively realized in the full atomistic simulations (Fig. 4B), with deviations from the analytical model arising primarily from the fact that finite H_x changes the equilibrium DW width Δ_0, which is not captured in the analytical model. The agreement between the atomistic simulations and the analytical treatment based on the sine-Gordon equation indicates that the assumptions in that model are justified and that the Lorentz invariance of its solitonic solutions captures the underlying physics. We therefore conclude that Lorentz contraction as v approaches v_g^{max} serves as the underlying cause of the limiting velocity in Fig. 2F and Fig. 4D.

Our results provide critical insight into the dynamical behavior of DWs at ultrafast velocities and demonstrate that magnetic systems under suitable conditions can serve as a laboratory platform for the relativistic kinematics of solitons. This may further enable the experimental observation of rare relativistic phenomena such as soliton dynamics in two- or three-dimensional systems, such as skyrmions under well-controlled conditions, and of solitons interacting dynamically with the lattice structure that is expected to mimic general relativity to a certain degree (*4*–*12*).

REFERENCES AND NOTES

1. A. Einstein, *Ann. Phys.* **322**, 891–921 (1905).
2. F. C. Frank, J. H. van der Merwe, *Proc. R. Soc. London* **198**, 205–216 (1949).
3. M. J. Rice, A. R. Bishop, J. A. Krumhansl, S. E. Trullinger, *Phys. Rev. Lett.* **36**, 432–435 (1976).
4. J. F. Currie, *Phys. Rev. A* **16**, 1692–1699 (1977).
5. M. B. Fogel, S. E. Trullinger, A. R. Bishop, J. A. Krumhansl, *Phys. Rev. B.* **15**, 1578–1592 (1977).
6. H. How, R. C. O'Handley, F. R. Morgenthaler, *Phys. Rev. B* **40**, 4808–4817 (1989).
7. F. D. M. Haldane, *Phys. Rev. Lett.* **50**, 1153–1156 (1983).
8. I. V. Bar'yakhtar, B. A. Ivanov, *Sov. Phys. JETP* **58**, 190–197 (1984).
9. S. K. Kim, Y. Tserkovnyak, O. Tchernyshyov, *Phys. Rev. B* **90**, 104406 (2014).
10. O. Gomonay, T. Jungwirth, J. Sinova, *Phys. Rev. Lett.* **117**, 017202 (2016).
11. T. Shiino *et al.*, *Phys. Rev. Lett.* **117**, 087203 (2016).
12. S.-H. Oh *et al.*, *Phys. Rev. B* **96**, 100407 (2017).
13. H. Y. Yuan, W. Wang, M.-H. Yung, X. R. Wang, *Phys. Rev. B* **97**, 214434 (2018).
14. W. Wang *et al.*, *Phys. Rev. Lett.* **114**, 087203 (2015).
15. N. L. Schryer, L. R. Walker, *J. Appl. Phys.* **45**, 5406–5421 (1974).
16. A. P. Malozemoff, J. C. Slonczewski, *Magnetic Domain Walls in Bubble Materials* (Academic Press, 1979).
17. L. Caretta *et al.*, *Nat. Nanotechnol.* **13**, 1154–1160 (2018).
18. E. Martínez, V. Raposo, Ó. Alejos, *J. Magn. Magn. Mater.* **491**, 165545 (2019).
19. G. S. D. Beach, C. Nistor, C. Knutson, M. Tsoi, J. L. Erskine, *Nat. Mater.* **4**, 741–744 (2005).
20. S.-H. Yang, K.-S. Ryu, S. Parkin, *Nat. Nanotechnol.* **10**, 221–226 (2015).
21. K.-J. Kim *et al.*, *Nat. Mater.* **16**, 1187–1192 (2017).
22. M. Yan, C. Andreas, A. Kákay, F. García-Sánchez, R. Hertel, *Appl. Phys. Lett.* **99**, 122505 (2011).
23. S. S. Parkin, M. Hayashi, L. Thomas, *Science* **320**, 190–194 (2008).
24. A. Fert, V. Cros, J. Sampaio, *Nat. Nanotechnol.* **8**, 152–156 (2013).
25. L. Soumah *et al.*, *Nat. Commun.* **9**, 3355 (2018).
26. I. M. Miron *et al.*, *Nature* **476**, 189–193 (2011).
27. L. Liu *et al.*, *Science* **336**, 555–558 (2012).
28. S. Emori, U. Bauer, S.-M. Ahn, E. Martinez, G. S. D. Beach, *Nat. Mater.* **12**, 611–616 (2013).
29. K.-S. Ryu, L. Thomas, S.-H. Yang, S. Parkin, *Nat. Nanotechnol.* **8**, 527–533 (2013).
30. A. Manchon *et al.*, *Rev. Mod. Phys.* **91**, 035004 (2019).
31. C. O. Avci *et al.*, *Nat. Mater.* **16**, 309–314 (2017).
32. C. O. Avci *et al.*, *Nat. Nanotechnol.* **14**, 561–566 (2019).
33. S. Vélez *et al.*, *Nat. Commun.* **10**, 4750 (2019).
34. A. Thiaville, S. Rohart, É. Jué, V. Cros, A. Fert, *Europhys. Lett.* **100**, 57002 (2012).
35. E. Martinez, S. Emori, N. Perez, L. Torres, G. S. D. Beach, *J. Appl. Phys.* **115**, 213909 (2014).
36. L. Caretta *et al.*, *Nat. Commun.* **11**, 1090 (2020).
37. O. Gaier *et al.*, *J. Phys. D Appl. Phys.* **42**, 232001 (2009).
38. J. Hamrle *et al.*, *J. Phys. D Appl. Phys.* **42**, 084005 (2009).
39. K. Matsumoto *et al.*, *Jpn. J. Appl. Phys.* **57**, 070308 (2018).
40. R. W. Damon, J. R. Eshbach, *J. Phys. Chem. Solids* **19**, 308–320 (1961).
41. S. O. Demokritov, B. Hillebrands, A. N. Slavin, *Phys. Rep.* **348**, 441–489 (2001).
42. L. Caretta *et al.*, Relativistic Kinematics of a Magnetic Soliton: Manuscript Data, version 01, Zenodo (2020); http://doi.org/10.5281/zenodo.4124678.

ACKNOWLEDGMENTS

Devices were fabricated using equipment in the MIT Microsystems Technology Laboratory. The authors thank L. Liu for use of the

ion milling equipment. The authors thank F. Büttner, J. Bartell, and B. Ivanov for helpful discussions and J. Bartell for preliminary BLS investigations. **Funding:** This work was supported by the DARPA TEE program and SMART, an nCORE Center. This work made use of the MIT Materials Research Science and Engineering Center (MRSEC) Shared Experimental Facilities, supported by the National Science Foundation under award number DMR-1419807. L.C. acknowledges financial support from the NSF Graduate Research Fellowship program and from the GEM Consortium. K.J.L. was supported by the Samsung Research Funding Center of Samsung Electronics under project no. SRFCMA1702-02. S.K.K. was supported by the Brain Pool Plus Program through the National Research Foundation of Korea funded by the Ministry of Science and ICT (grant no. NRF-2020H1D3A2A03099291). **Author contributions:** L.C., C.A.R., and G.S.D.B. conceived the project and planned the experiments. T.F. synthesized and characterized BiYIG films. L.C. performed VSM, deposited the metal layers and microfabricated the DW tracks, prepared the experimental setup, and performed the DW measurements. Numerical modeling was performed by S.-H.O. and D.-K.L. B.H.L. performed BLS experiments and analysis. Analytical modeling was performed by S.K.K., K.-J.L., G.S.D.B., and L.C. L.C. and G.S.D.B. wrote the manuscript with input from S.K.K., K.-J.L., and C.A.R. All authors contributed to the discussion of the data in the manuscript and the supplementary materials. **Competing interests:** The authors declare no competing interests. **Data and materials availability:** All data presented in the paper and the supplementary materials are open access and can be found on Zenodo (*42*).

SUPPLEMENTARY MATERIALS

science.sciencemag.org/content/370/6523/1438/suppl/DC1
Materials and Methods
Supplementary Text
Figs. S1 to S6
References (*43*–*65*)

12 December 2019; resubmitted 19 May 2020
Accepted 13 November 2020
10.1126/science.aba5555

Relativistic kinematics of a magnetic soliton

Lucas Caretta, Se-Hyeok Oh, Takian Fakhrul, Dong-Kyu Lee, Byung Hun Lee, Se Kwon Kim, Caroline A. Ross, Kyung-Jin Lee and Geoffrey S. D. Beach

Science **370** (6523), 1438-1442.
DOI: 10.1126/science.aba5555

Magnetic special relativity

Magnetic materials have domains, patches of ordered spins that are separated from one another by boundaries called domain walls. These boundaries can be driven by electrical currents, a phenomenon forming the basis of the so-called racetrack memories. The speed of the domain walls has steadily increased as experimenters have perfected these devices. Caretta *et al.* now show experimentally that this speed is fundamentally limited (see the Perspective by Daniels and Stiles). Just as no object can travel faster than the speed of light, the speed of the domain walls saturates to a constant determined only by the properties of the magnetic host material.

Science, this issue p. 1438; see also p. 1413